scientific reports

Check for updates

OPEN

Development of a fully packaged passive thermal regulator

Seung Won Park[1], Junhui Li[1] & Patricia B. Weisensee[1,2]✉

Thermal regulators are devices that can adopt either the role of a thermal insulator or a thermal conductor, depending on the thermal input conditions, and play an increasingly important role in thermal management systems. In this study, we developed and tested a new passive thermal regulator design that operates around room temperature and achieves high switching ratios. Our regulator is structurally integer, scalable, orientation-independent, resistant to vibration, and can be easily integrated into existing thermal management solutions. The working principle of the passive regulator is simple yet effective, whereby an aluminum plug attached to a bimetallic strip enters and exists a wedge-shaped gap between two conductors. We demonstrate a switching ratio of ≈ 50 ($^{+34}_{-8}$):1 for a fully packaged prototype (≈ 320 (± 200):1 for a non-packaged regulator) operated in the open laboratory environment. Through geometric optimization using numerical simulations, we show that a switching ratio of ≈ 100 ($^{+18}_{-15}$):1 can be easily obtained, which can be further increased by increasing the cross-sectional area of the input conductor, hence increasing the ON-state heat transfer rate. The OFF-state thermal performance is much less sensitive to the size of the conductor, making the device highly scalable.

Thermal regulators are becoming increasingly popular as adaptive components in thermal management systems, including electronics and battery thermal management[1–3], refrigeration[4–6], space applications such as satellites and rovers[7], and even building envelopes[8]. Analogous to electrical regulators, which allow or prevent current from flowing through a circuit, thermal regulators are able to manipulate the flow of thermal energy, i.e., heat, between a warmer source and a colder sink. They adopt either the role of a good conductor ("ON") or a good insulator ("OFF"). One of the key parameters to evaluate the performance of a thermal regulator is its switching ratio (*SR*), which relates the thermal conductances *C* in the ON and the OFF-states: $SR = C_{ON}/C_{OFF}$. A high switching ratio, a high ON-state heat flux, a low specific mass, and a small volumetric footprint are desirable for most applications.

Over the past 50+ years, many thermal regulator designs have been proposed to manipulate the flow of heat[9,10], most of which fall into one of the two categories: Active or passive. In passive thermal regulators, the change in effective conductance depends solely on the temperature or applied thermal load and does not require active manipulation or control of the device. As an example, the regulator can be fully ON at a temperature T_{ON} above the transition temperature T_t and fully OFF for $T_{OFF} < T_t$. Actively controlled regulators, also called heat switches, have a more versatile operating range, but require additional external triggers, such as electric or magnetic fields[11–18], mechanical actuation (e.g., via compression, displacement, or gravitational re-orientation)[19–23], or pumps, compressors, or fans[24,25] to operate. This manuscript focuses on passively actuated thermal regulators operating around room temperature (i.e., ignoring gas-gap regulators for cryogenic applications[26–28]) for use in stationary or remote applications with passive thermal management requirements.

The earliest passive thermal regulators were developed primarily for space applications, such as missions to the moon or Mars[29,30]. Many of these regulators were paraffin-based, whereby the volumetric expansion of paraffin wax upon melting (up to 15%) brings two thermal conductors into mechanical contact, thereby closing the thermal loop. Paraffin-based regulators are durable, low cost, and have no material compatibility issues, making them popular to this date[31–37]. By adjusting the molecular chain length of the paraffin wax, the actuation temperature can be set between − 95 and + 85 °C and switching ratios up to 130:1 have been achieved (though most designs have practical $SR << 100$). Alternative designs replace the paraffin and the metallic actuator with an all-solid material assembly. Examples include shape memory alloys, bimetallic strips, or rods with high coefficients of thermal expansion (CTE)[7,38–41]. Some of these designs have a significantly smaller volumetric footprint than paraffin regulators, albeit at the cost of a lower switching ratio[19,42]. High switching ratios > 100:1 can also be achieved by room-temperature gas-gap regulators, whereby an increase in temperature releases gas from a sorber material into a thin gap (O(100 μm)), thereby increasing the thermal conductivity of the gap[43]. Instead of using gas as the

[1]Department of Mechanical Engineering and Materials Science, Washington University in St. Louis, St. Louis, MO, USA. [2]Institute of Materials Science and Engineering, Washington University in St. Louis, St. Louis, MO, USA. ✉email: p.weisensee@wustl.edu

heat transfer fluid, two-phase thermal regulators take advantage of very high effective conductivities during the absorption and release of latent heat on the source and sink sides of the regulator, respectively, of phase-change working fluids upon reaching saturation conditions at a certain temperature[44]. Switching ratios are nonetheless modest due to parasitic losses in the system[45,46]. Moderate switching ratios < 30:1 have also been demonstrated for solid state materials which undergo magnetic phase transformations with changes in temperatures[47,48]. For an in-depth overview of other passive and active thermal control technologies, we would like to refer the interested reader to two recent reviews by Klinar and colleagues[4,10]. Despite the wealth of different designs and actuation mechanisms, most existing passive regulating technologies suffer from at least one of the following challenges: A low switching ratio ($SR < 100$), especially for fully packaged and integrated designs and measured in an open atmosphere (as opposed to a vacuum chamber), a complex actuation mechanism, a small heat transfer area, poor scalability, and/or a high volumetric aspect ratio and bulky design.

To overcome existing shortcomings, we designed a passive thermal regulator that has a high switching ratio in an open environment, is fully packaged and structurally integer, is scalable, and is able to withstand vibrations or impact during operation, for example for applications in lunar rovers or off-road vehicles. Figure 1 shows the working principle of our device. It consists of two copper blocks, each cut at an angle (60° from the vertical), into which an aluminum trapezoid is inserted. Copper was used for these two static blocks due to its high thermal conductivity (398 W/m K). Aluminum was chosen as the dynamic actuator block, instead of copper, due to its superior thermal conductance per unit mass (87 (W/m K)/(g/cm^3) for aluminum vs. 45 (W/m K)/(g/cm^3) for copper). However, to further improve the ON-state thermal performance, copper could also be used as the actuator block at the cost of a higher switching hysteresis. Similarly, the input and output blocks could be made of aluminum or another material with smaller density to decrease the overall weight of the assembly, at the cost of a slight reduction in the thermal performance. In our prototype, the aluminum actuator is connected to one of the copper blocks, namely the input block, via a bimetallic strip. A bimetallic strip consists of two metal films with different thermal expansion coefficients bonded together. When the temperature of the bimetallic strip is changed, in the absence of external forces, the assembly takes the shape of an arc. The metal with a larger thermal expansion is known as the active element, while the metal having the smaller coefficient of expansion is called the passive element[49]. For our thermal regulator design, the active element is facing away from the assembly and one end of the bimetallic strip is attached to the input copper block. Therefore, the other end of the strip, which has the aluminum plug attached to it, deforms upward when cooled and downward when heated. Specifically, when the temperature of the input copper block T_{in} is higher than 25 °C (in the orientation shown in the figure), the bimetallic strip bends downward and pushes the aluminum plug into the gap, thereby allowing the flow of heat between the two copper blocks and turning the device ON. At temperatures below ≈ 15 °C, the strip is fully bent upward, and the aluminum plug is completely removed from the gap. Any heat flow between the two copper blocks is greatly diminished and the regulator is OFF. The geometry of the aluminum block was optimized to ensure seamless actuation without jamming and to minimize its mass, which ensures that the thermal performance is nearly orientation-independent.

Experimental methods

Thermal regulator design and experimental setup

Figure 2 shows a schematic of the primary experimental setup used for the full thermal characterization of the regulator. The cold plate on the bottom functioned as a heat source during the ON-state measurement and as a heat sink during the OFF-state measurement. A coolant (50% water/50% glycerol), circulating through a chiller

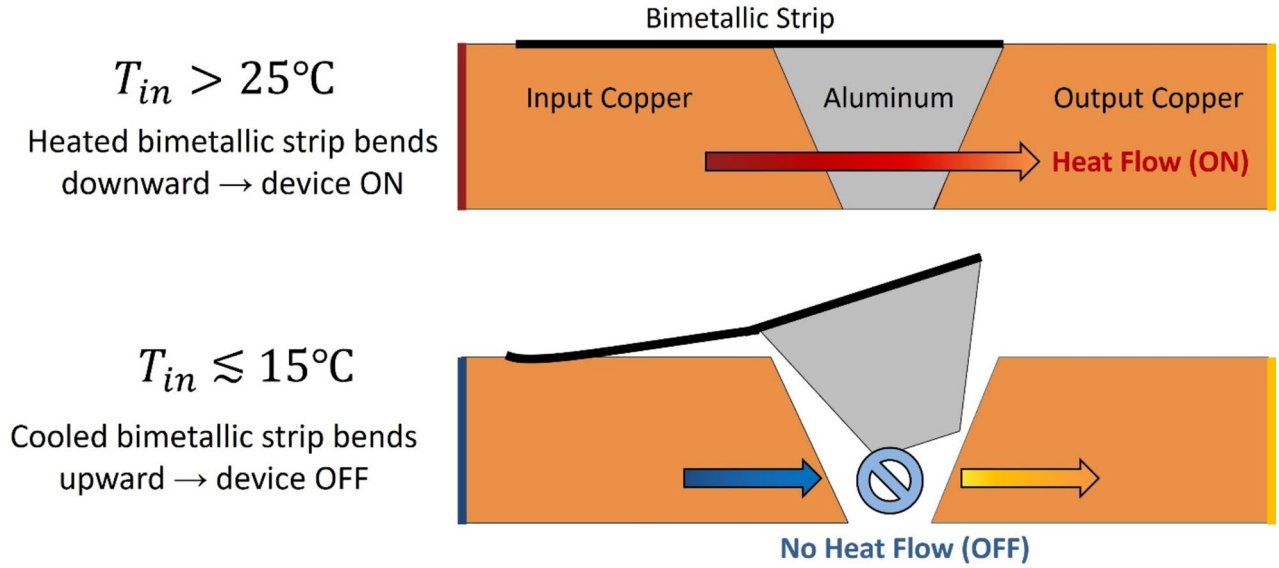

Figure 1. General concept of the passive thermal regulator.

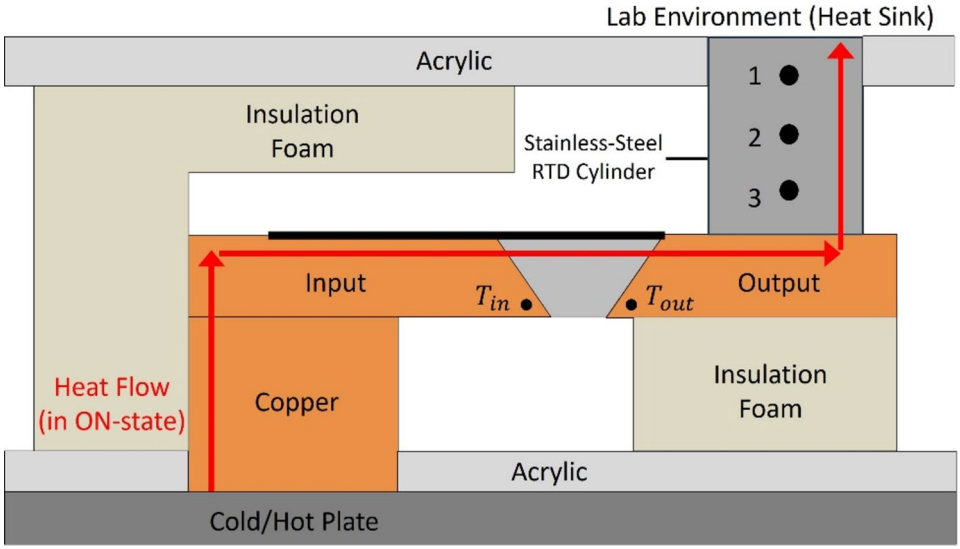

Figure 2. Schematic of the experimental setup of the primary prototype.

(AD07R-40-A11B, PolyScience), was connected to the fluid inlet and outlet ports of the cold plate, providing an approximately constant-temperature boundary condition to the input side of the regulator. Two acrylic sheets (84 mm × 165 mm × 3/8"; McMaster) were used to ensure the structural integrity and "plug-and-play", i.e., drop-in functionality of the regulator assembly: one was directly placed on the cold plate and the other one was on the top side of the regulator, supported by an L-shaped polyurethane insulation foam block, and open to the environment. Polyurethane was chosen for the insulator due to its low thermal conductivity (< 0.03 W/m K), structural integrity, and durability. Another polyurethane insulation foam (64 mm × 54.33 mm × 15.48 mm; amazon.com) was placed between the output copper block and the acrylic sheet to provide structural support while minimizing parasitic heat conduction from the cold plate through the regulator (especially in the OFF-state). On the input side, a rectangular hole was cut into the acrylic sheet to accommodate a copper block (64 mm × 25 mm × 25 mm; OnlineMetals.com) that supported and thermally connected the input side of the regulator to the cold plate. The two copper blocks (support and regulator) were attached to each other with a thermal conductive glue (Easycargo, ES-910) to reduce the thermal contact resistance and to improve the structural integrity. Two stacked sheets of bimetallic strip (64 mm width × 75 mm length, Kanthal 200, Huona Shanghai) were attached to the other side of the input copper block, also using thermal glue. The aluminum trapezoid attached to the other end of the bimetallic strips had a bottom width of 16.34 mm (angle: 60°) and a height of 7.5 mm (raw material purchased from OnlineMetals.com).

At the output side of the regulator, a stainless steel cylinder (height: 70 mm, diameter: 44.5 mm; McMaster) was used to connect the output copper of the regulator to the open lab environment ($T_{env} \approx 22.3$ °C; again through a hole cut into the acrylic sheet), which acted as a heat sink. Three resistance temperature detectors (RTDs) (Pt100, 2″ long, 1/8″ diameter probe; Evosensors), from which the heat flux through the device could be determined, were inserted into three equidistant holes (spacing: 17.5 mm) in the steel cylinder. The procedure for RTD calibration is described in the Supplementary Information, Section S1. Thermal compound (Arctic MX-4) ensured a good thermal contact between the RTDs and the steel cylinder. We used stainless steel ($k \approx 16.5$ W/m K) instead of copper ($k \approx 390$ W/m K) to decrease the uncertainty of the heat transfer measurement. Two surface RTDs with adhesive backing (EvoSensors) were mounted on the input and output copper blocks on either side of the aluminum plug to measure the temperature drop across the plug (ON) or gap (OFF). To minimize the thermal contact resistance between the aluminum plug and the two copper blocks, we applied a thin layer of the thermal compound between the interfaces. The thermal compound has a viscosity of 31.6 poise and the bending force exerted by the bimetallic strip when transitioning into the OFF-state was strong enough to overcome the compound's resistance and pull the aluminum plug out of the gap. The effect of applying thermal compound between interfaces on the thermal performance is summarized in Supplementary Information, Section S2. Most metal surfaces, except the top face of the stainless steel cylinder, were covered with additional stick-on insulation to minimize heat losses to the environment.

In addition to the primary prototype used for the full thermal characterization of the thermal regulator, we also fabricated a second, fully packaged device, in which the stainless steel cylinder on the output side was replaced with another copper block, as shown in Fig. 3. The dimensions were also adjusted to strike a balance between thermal performance and compactness. The updated design had a total footprint of 165 mm length, 84 mm width and 57.5 mm height. The thermal regulator assembly was fully enclosed with acrylic sheets for structural integrity, better insulation, and full system integration capabilities (i.e., in addition to the bottom and top plates of the primary prototype, this second prototype also had four vertical plates). This design change also allowed us to characterize the device performance in different orientations. As the two extremes, we quantified

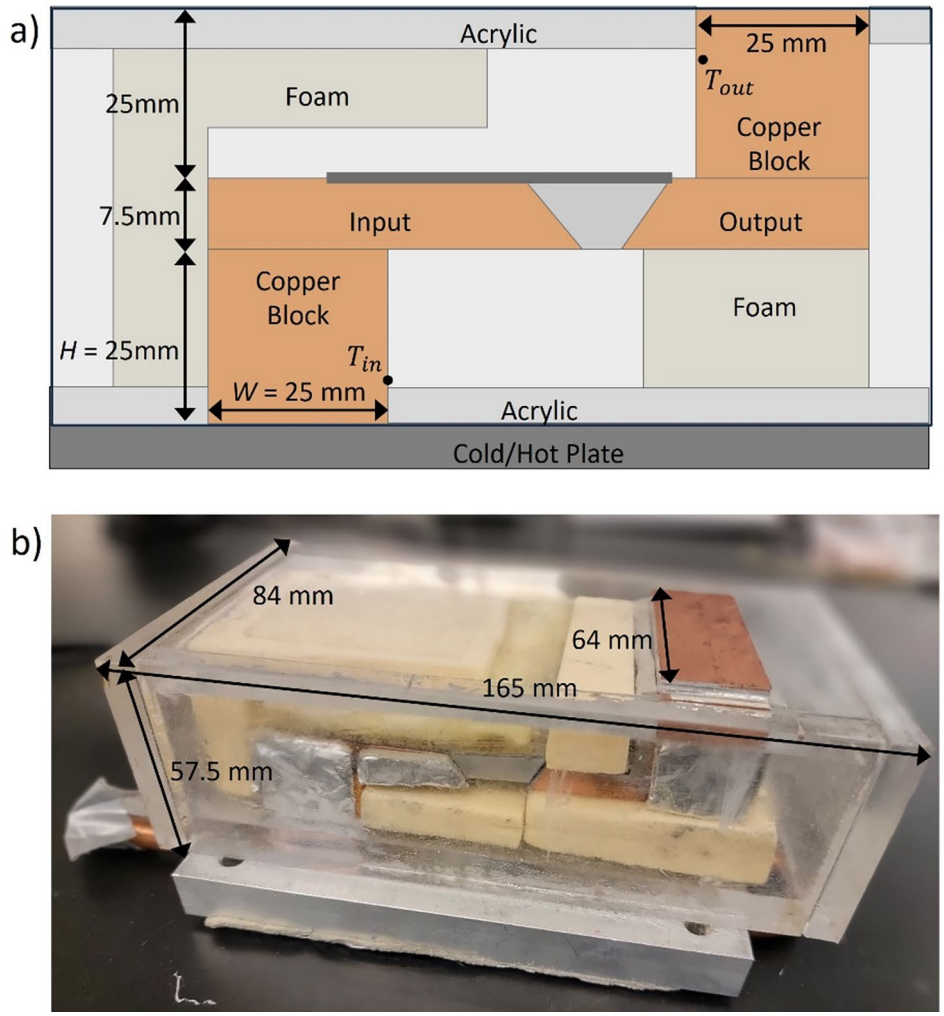

Figure 3. Schematic (**a**) and image (**b**) of the fully packaged prototype on the cooling/heating plate.

the thermal performance with the bimetallic strip facing up (as shown in the schematic) and with the strip facing down (i.e., flipped by 180°). The thermal performance of other orientations is expected to lie in-between these two configurations. The second prototype had only two temperature measurement locations, with two surface RTDs located at the supporting copper blocks of the input and output side, respectively, close to the acrylic plates, as indicated in the schematic in Fig. 3. While heat flux measurements were not possible with this setup, it allowed us to develop T_{in}-vs.-T_{out} correlations that are more realistic for an actual regulator used in an application.

Thermal analysis

For the thermal characterization of the primary prototype, the chiller temperature was set between − 20 °C and 60 °C, with 10 °C increments (5 °C for the fully packaged prototype). The corresponding cold plate/hot plate temperatures were slightly higher/lower, due to heat transfer to the environment. At each set-point, temperatures at the five different locations (input, output, three RTD cylinder temperatures) were recorded using a RTD data logger (Madgetech, OCTRTDTEMPV2 Data Logger) in 10 s time intervals once the entire system had come to thermal equilibrium. From the temperature measurements, the heat transfer rate q (W) was calculated using Fourier's law of conduction in a 1D medium:

$$q = \left| kA \frac{\Delta T}{\Delta x} \right|, \tag{1}$$

where A is the cross-sectional area of the stainless-steel cylinder (0.0016 m^2), k is the thermal conductivity of the stainless steel (16.5 W/m K), and $\Delta T/\Delta x = (T_1 - T_3)/(2 \times 17.5\ \text{mm})$ is the temperature gradient within the steel cylinder, where T_i correspond to the respective RTD locations indicated in Fig. 2. The data point T_2 was used to evaluate the linearity in the temperature gradient (for all cases, the R^2-value from a linear regression fit was greater than 0.96). Figure 4 shows the measured temperatures for a chiller temperature of − 20 °C (OFF-state) and a chiller temperature of + 60 °C (ON-state). Due to the shallow temperature gradient, especially in

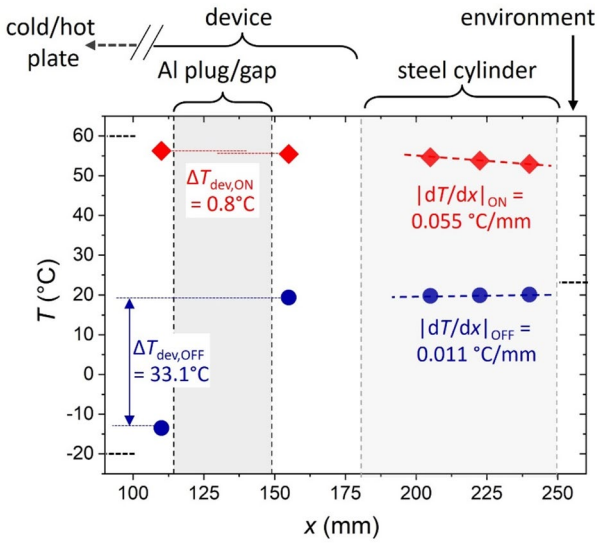

Figure 4. Exemplary temperature profiles for the ON- and OFF-states.

the OFF-state, the uncertainties in the heat flux are $U_{q,ON} \leq 0.21$ W and $U_{q,OFF} \leq 0.096$ W, respectively. Details on the uncertainty analysis are given in the Supplementary Information, Section S3.

With the heat transfer rate, the thermal conductance C (W/K) can be calculated as:

$$C = \frac{q}{|\Delta T_{dev}|} = \frac{q}{|T_{in} - T_{out}|}, \tag{2}$$

where T_{in} and T_{out} are the temperatures of the input and the output copper blocks, as measured by the surface RTDs, respectively, representing the temperature change across the regulator (or device, ΔT_{dev}). Using Eq. (2), the ON-state thermal conductance, C_{ON}, and the OFF-state thermal conductance, C_{OFF}, are obtained. Finally, the switching ratio becomes:

$$SR = \frac{C_{ON}}{C_{OFF}}. \tag{3}$$

The uncertainties in the conductances and the switching ratio are $U_{C,ON} \leq 0.08 \ldots 0.30$ W/K, $U_{C,OFF} \leq 5$ mW/K, and $U_{SR} = 200$, respectively.

In addition to determining the switching ratio to evaluate the performance of the regulator, we also compared the difference in the output to the environmental temperature ($|\Delta T_{out}| = |T_{out} - T_{env}|$) as a function of the total thermal driving force (i.e., the absolute difference between the input temperature and the environmental temperature, $|\Delta T_{in}| = |T_{in} - T_{env}| \approx 0 \ldots 40$ °C). T_{env} is the environmental temperature in the laboratory, which was approximately 23 °C. A good thermal regulator is expected to (1) restrict the heat flow across the device and maintain the output temperature close to the environmental temperature in the OFF-state, and (2) enable heat flow across the device and bring the output temperature close to the input temperature in the ON-state. Thus, the goal is to minimize the temperature drop across the device, $|\Delta T_{dev}|$, in the ON-state and maximize it in the OFF-state. This is equivalent to maximizing the difference between $\Delta T_{out,ON}$ and $\Delta T_{out,OFF}$. In fact, due to the high uncertainty of heat flow measurements in the OFF state, the output temperature difference $|\Delta T_{out}|$ between ON and OFF states might be a better metric to characterize the thermal device performance than the switching ratio, and will be used to evaluate the performance of the fully packaged prototype.

Results and discussion

Actuation performance of the thermal regulator

Figure 5 shows images of the actuation mechanism upon cooling and heating of the first prototype in its normal (i.e., upright) orientation (Fig. 5a) and flipped (i.e., upside-down) orientation (Fig. 5b). At temperatures slightly above room temperature the plug firmly rests within the wedge created by the two copper blocks and the regulator is in its ON position. Upon cooling of the input side (left side of the setup), the bimetallic strip bends upwards, pulling the aluminum plug out from the gap and turning the regulator OFF, which for both prototypes occurs for $T_{in} \lesssim 15$ °C. At this stage, it is important that the aluminum plug is fully withdrawn from the wedge, that is, that there is an air gap present even at the bottom tip of the aluminum plug. This condition can be achieved through geometric optimization. Upon heating ($T_{in} > 25$ °C), the bimetallic strip bends downwards again, closing the regulator and turning it ON. When operating the device upside-down, i.e., with the bimetallic strip mounted at the bottom of the input copper block, the same principle can be observed, but temperature limits are shifted.

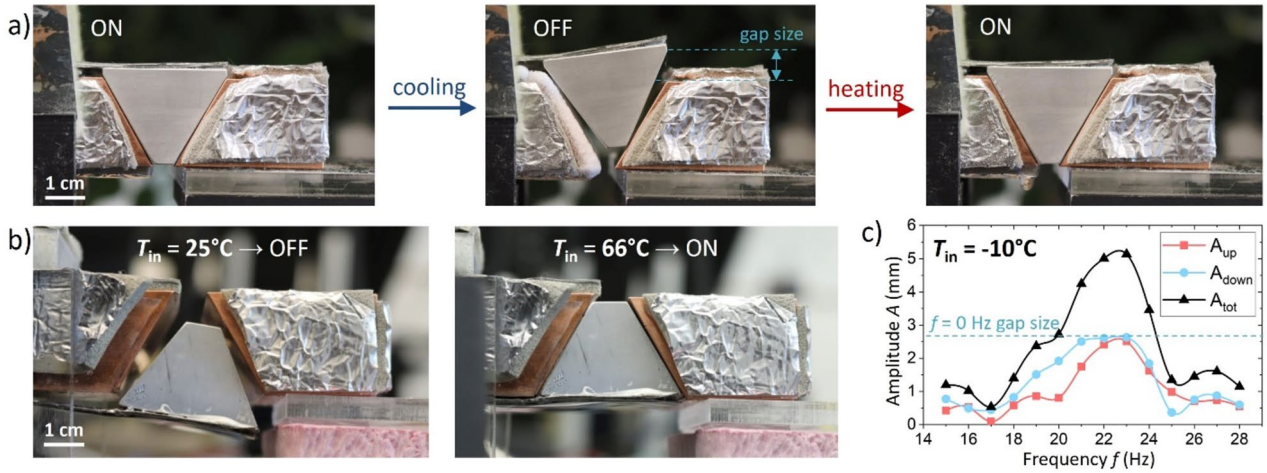

Figure 5. Demonstration of the actuation mechanism. (**a**) Full cooling and heating cycle for the first prototype in its upright orientation. (**b**) OFF and ON-states for the first prototype for an upside-down orientation. (**c**) Amplitude of deflection of the aluminum plug tip of the second, fully packaged prototype upon vibration at different frequencies. The blue dashed line represents the gap height at rest in an upright position and at an inlet temperature of $T_{in} = -10$ °C, i.e., it shows the maximum possible amplitude in the downward direction.

Due to the weight of the aluminum block, the plug is withdrawn from the wedge at room temperature (and below) and does not turn ON until the input temperature reaches ≈ 65 °C (≈ 30 °C for the compact prototype).

To demonstrate the robustness of our device, we also tested its resilience to external vibration. We mounted the fully packaged prototype with the cold plate temperature set to − 10 °C on a vibrator system (Vibration Test Systems, VG 100-6) and measured the deflection of the bimetallic strip for sinusoidal actuation frequencies between $f = 10$ and 35 Hz. The signal amplification remained the same for all frequencies, resulting in a total actuation amplitude 0.1…0.4 mm of the assembly. Figure 5c shows the amplitude response of the strip tip for $f = 15…28$ Hz. The blue dashed line represents the distance between the strip tip and the copper output block at rest, i.e., the equilibrium gap size. The blue data points show the downward deflection of the strip and the red curve the upward deflection with respect to its static equilibrium. The black line is the total travel distance of the aluminum plug, which we call the total response amplitude. It reaches a maximum of ≈ 5 mm at a frequency around 22 to 23 Hz, indicating resonance. At this actuation frequency, the plug temporarily comes into full contact with the output copper block. The influence of this temporary closing of the regulator on its OFF-state thermal performance will be discussed in more detail in "Influence of orientation and vibration on the thermal performance" section.

Thermal characterization of the thermal regulator

After demonstrating the successful passive actuation of the regulator, we now turn to quantifying its thermal response. Figure 6a shows the output temperature along with the measured thermal conductances of the primary prototype as a function of the input temperature according to the measurement locations indicated in Fig. 2. For an ideal thermal regulator, in the OFF-state the output temperature would be constant at the environmental temperature, irrespective of the input temperature, i.e., the output side would be entirely thermally isolated from the input. In reality, there are some parasitic heat losses through the assembly, which can be reduced by geometric and operational optimization. In the ON-state, an ideal regulator would have no thermal resistance between the inlet and the outlet, i.e., the output temperature would be the same as that of the input. Our regulator achieved an extremely good ON-state efficiency, with $T_{out} \approx 0.97\ T_{in}$. This can be thought of like a thermal diode, where a forward bias ($T_{in} > T_t$) allows heat to flow (analogous to current in an electrical diode), but a reverse bias ($T_{in} < T_t$) inhibits heat transfer.

From temperature measurements in the stainless steel cylinder, along with Eqs. (1) and (2), the heat flow and conductance, respectively, through the regulator can be determined. The heat flow through the assembly was between 0.02 W for a cold plate temperature near room temperature and 1.2 W for a hot plate temperature near 60 °C, and is plotted in Fig. 6b (hollow symbols) as a function of the thermal driving force $\Delta T_{in} = |T_{in} - T_{env}|$ (for our electrical diode analogy, this would be the applied voltage). The figure also includes $|\Delta T_{dev}|$ (filled symbols) and the resulting thermal conductances. The OFF-state is marked by the blue circles and the ON-state by red diamonds. Black and gray squares represent the transition regime. In the OFF-state, the average conductance is $C_{OFF} \approx 5\ (\pm 3)$ mW/K, whereas ON-state conductances varied between 0.16 (± 0.08) and 1.52 (± 0.30) W/K, depending on the input temperature, which leads to a maximum switching ratio of $SR_{max} = 320\ (\pm 200)$:1. The relatively high uncertainty in the switching ratio stems primarily from the shallow temperature gradient in the OFF-state heat flux measurement seen in Fig. 4.

Figure 7a shows the temperature response for the fully packaged device. The general trend is the same as for the primary prototype, but parasitic heat losses through the encapsulation and support structures are more pronounced, leading to an up to 10 K temperature deviation from the environment in the OFF-state (for the primary

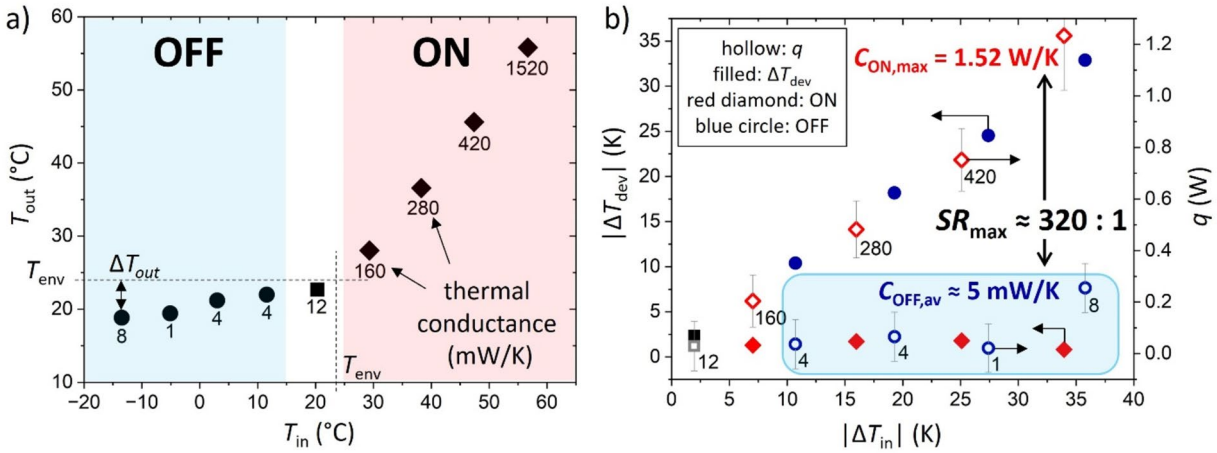

Figure 6. Thermal performance of the primary prototype. (**a**) Output temperature as a function of input temperature, as measured in the copper blocks directly adjacent to the aluminum plug. The regulator is fully OFF for input temperatures below 15 °C and fully on for $T_{in} \geq 25$ °C. The thermal conductances are also given and are characterized by $C_{OFF} < 10 \pm (3 \ldots 9)$ mW/K and $C_{ON} \sim 0.1 \ldots 1.5 \pm (0.08 \ldots 0.34)$ W/K. (**b**) Heat flow (hollow symbols) and temperature difference across the regulator (filled symbols) as a function of the input thermal driving force. Blue circles represent the OFF-state and red diamonds the ON-state. Black and gray squares represent the transition regime. At $\Delta T_{in} \approx 35$ °C, the regulator achieves a switching ratio $SR \approx 320$ (± 200):1.

prototype, $|\Delta T_{out,OFF}| \leq 5$ K). In the ON-state, the performance is again almost ideal, i.e., with very few heat losses along the thermal path, with $T_{out} \approx 0.95\ T_{in}$. This prototype did not include a stainless steel cylinder, so the heat fluxes, conductances and switching ratio cannot not be determined directly. Instead, we turn to the overall temperature response (especially $|\Delta T_{out,ON}|$ vs. $|\Delta T_{out,OFF}|$) to evaluate the effectiveness of the device and see that our prototype outperforms many existing technologies that operate in an open environment around room temperature and are fully packaged (i.e., structurally integer)[11,20,40,48]. If we nonetheless want to estimate a switching ratio for the ease of comparison, we can either turn to an indirect experimental approach or use numerical analysis, both of which are discussed below. If we assume that the total heat flow for this prototype is the same as for the primary prototype at any given input temperature (i.e., $q \approx 1.20$ W at $T_{in} = 57$ °C and $q \approx 0.20$ W at $T_{in} = -12$ °C), then we can estimate the switching ratio of the packaged prototype to be $SR \approx 40$:1. The assumption of similar heat flow between the two prototypes can be reasonably well justified: In the ON-state, the important factors influencing the total transferred heat are (1) the cross-sectional area of the input copper block, (2) the thermal conductivity of the metals, and (3) the input-to-environment temperature difference; all three are the same for both prototypes. In the OFF-state, the net heat transfer is also governed by the cross-sectional areas of the copper blocks, the thickness of the insulation foam between the output side and the cold plate (via parasitic conduction), and convective heat transfer within the enclosure. The latter is different between the two prototypes, with the primary prototype being fully open to the lab environment and the packaged prototype being fully enclosed. Minor differences in heat flow rates are thus likely, but we expect this switching ratio estimate to nonetheless be of the right order. This assumption is supported by COMSOL simulations, which indicate a switching ratio of $\approx 50\ (^{+34}_{-8})$:1 for the fully packaged prototype ($C_{ON} = 0.44$ W/K and $C_{OFF} = 8.7$ mW/K). Details on the numerical simulations are given in the Supplementary Information, Section S4. The switching ratio can be further increased through geometric optimization, as will be discussed in more detail in "Geometric optimization" section.

We also characterized the dynamic temperature response of the regulator. For this, we used two recirculating chillers; one set to − 10 °C and the other set to + 50 °C, which were sequentially attached to the cold/hot plate during the experiment. Figure 7b shows the temperature at the input and output sides as a function of time. Measurements started once the setup reached steady state in the OFF-state ($T_{in} \approx -8$ °C). Then, the circulating coolant in the cold/hot plate of the setup was changed to the chiller set to + 50 °C. The chillers had to be temporarily turned off to exchange the tubing, which caused a small drop in temperature and a short time delay in reaching 50 °C again. Once the input temperature reached + 25 °C, the bimetallic strip started moving downward, pushing the aluminum plug into the wedge. We define the rise in output temperature due to heat conduction through the aluminum plug as the conclusion of the switching process, which took less than 10 min to transition from fully OFF to fully ON. Once the output temperature approached its steady-state value, we exchanged the tubing again and attached the chiller set to − 10 °C. The switching from ON to OFF was even faster, taking less than 5 min to fully exit the aluminum plug from the wedge. The subsequent decrease in output temperature was much more gradual than during heating, though, since it relied on natural convection and some parasitic heat conduction through the enclosure, which are inherently slow. Overall, while the actuation timescales are longer than for some other technologies, such as devices based on electrowetting or magnetic switching[12,15,16], they are still satisfactory due to the much longer thermal constants of heat conduction and dissipation.

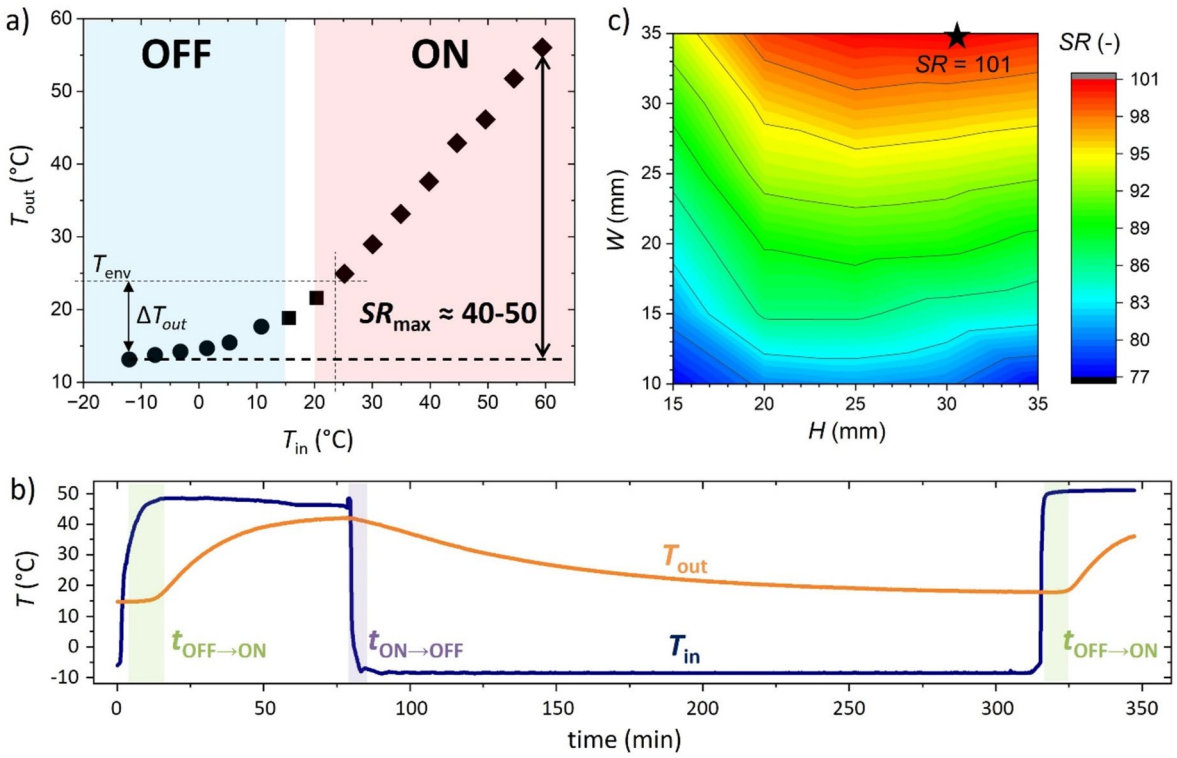

Figure 7. Thermal performance of the fully packaged prototype. (**a**) Output temperature as a function of input temperature, as measured in the supporting copper blocks adjacent to the cold/hot plate and the surface exposed to the environment, respectively. The regulator is fully OFF for input temperatures below 15 °C and fully on for $T_{in} \geq 20$ °C. Thermal conductances were not measured due to the lack the stainless steel cylinder. The switching ratio was estimated from heat flow measurements of the primary prototype and numerical simulations. (**b**) Dynamic temperature response of the regulator as the input temperature changes from ≈ − 8 °C to ≈ + 48 °C. Switching, i.e., the movement of the actuator, is very fast for the ON → OFF transition (< 5 min) and has a slight delay (≈ 8–10 min) for the OFF → ON transition. The temperature response is more gradual due to the slow evolution of conduction (→ ON) and natural convection (→ OFF). (**c**) Estimated switching ratio using numerical simulations for variations in the input copper block dimensions (width W and height H) for an output copper block with W = 25 mm, H = 12.5 mm and a constant depth of 64 mm.

Influence of orientation and vibration on the thermal performance

To quantify the robustness of our regulator design against outside influences, such as orientation and vibration, we tested the fully packaged prototype upside-down, where the bimetallic strip was at the bottom of the copper blocks and the weight of the aluminum plug caused the regulator to be OFF at room temperature. Figure 8a shows the thermal response in the flipped orientation, where we can see that the regulator turned ON at $T_{in} \approx 28 \ldots 30$ °C (as opposed to ≈ 20 °C for the original orientation). A device tilted sideward is expected to have a switching temperature between the two extremes of an upward and downward facing bimetallic strip.

To test the robustness of the regulator to mechanical vibration, for example, for use in off-road vehicles or other non-stationary applications, we characterized the OFF-state thermal performance at a vibration frequency of 22 Hz—close to the resonance frequency of the regulator. The mechanical analysis discussed in "Actuation performance of the thermal regulator" section and shown in Fig. 4c revealed that at these conditions, the aluminum plug temporarily fully closes in each vibration cycle. This cyclic closing of the regulator leads to an overall slight decrease in the output temperature, as shown in Fig. 8b. At an input temperature of $T_{in} = -8.3$ °C, the output temperature decreases from $T_{out} = 15.7$ °C at rest to $T_{out} \approx 13$ °C upon vibration—representing a continued high level of thermal insulation in the OFF-state.

Geometric optimization

Our fully packaged prototype showed a switching ratio of approximately 40–50 $(^{+34}_{-8})$:1, which is on par with many existing technologies (some of which require operation in vacuum to minimize heat transfer in the OFF-state). In order to demonstrate the capabilities and limits of our new regulator design, we turned to numerical simulations using COMSOL Multiphysics to explore a larger design space than is feasible using experimentation. We primarily explored the influence of input and output copper block dimensions and found that the width of the input copper block and the height of the output copper block played dominant roles in the thermal performance (interestingly, the height of the input copper block played a minor role). Figure 7c shows a color map

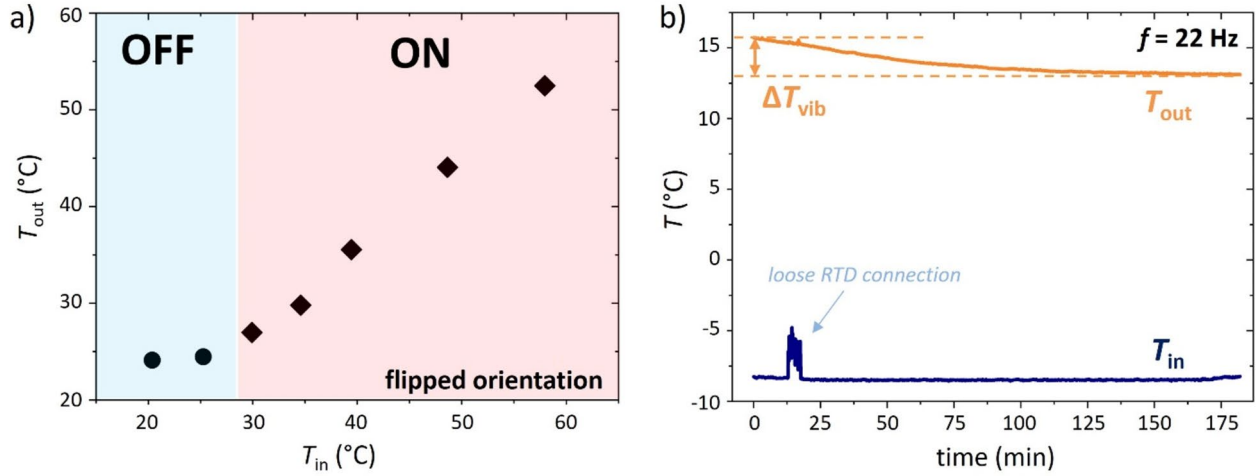

Figure 8. Thermal performance of the fully packaged setup when (**a**) flipped upside-down, i.e., with the bimetallic strip on the bottom side, and (**b**) subject to vibration near its resonance frequency around 22 Hz (regular orientation) when nominally OFF. When flipped, the regulator turns fully ON at a slightly higher input temperature of $T_{in} \approx 30$ °C. When vibrating at a frequency and amplitude that temporarily brings the aluminum plug and copper wedge into contact, the output temperature decreases slightly due to conduction through the regulator. The artificial spike in T_{in} around 15 min was caused by a loosened contact of the RTD during vibration.

of the predicted switching ratio as a function of the input copper width W and height H (output copper block dimensions in this figure were $W = 25$ mm and $H = 12.5$ mm). Within the design space we explored, the highest switching ratio we obtained for the fully packaged regulator was $SR = 101\ (^{+18}_{-15})$ for an input copper block width and height of 35 mm and 30 mm, respectively, as indicated by the star (the depth was held constant at 64 mm). This design also included a change in the shape of the foam insulation from a solid cuboid in the experimental conditions to a bridge geometry to minimize parasitic conduction losses during OFF-state operation. Overall, however, the higher switching ratio was obtained primarily through an increase in the ON-state conductance rather than a decrease in the OFF-state conductance, which can be achieved by increasing the cross-sectional area of the input copper block, indicating good feasibility for scale-up.

Given the potential use of the passive thermal regulator in mobile and space applications, the gravimetric, i.e., weight-normalized performance of the device is important. We therefore also explored the influence of geometry and material on the gravimetric switching ratio, SR/m, where m is the total mass of the device. By changing the copper components to aluminum, which has a much lower density (albeit at the cost of a slightly lower thermal conductivity), we obtained a gravimetric switching ratio of $SR/m = 247$ kg^{-1} (input aluminum block width and height 15 mm and 20 mm, respectively). Generally, in order to maximize the gravimetric switching ratio, short and narrow input and output blocks are preferred.

Additional results from geometric optimization studies, including the influence of the foam insulation shape and variations in input and output copper block sizes are discussed in more detail in Supplementary Information, Section S5.

Estimated lifetime of the thermal regulator

The lifetime of the thermal regulator as a dynamic system is dictated by the lifetime of the individual actuator components: the bimetallic strip and the reliability of its thermal bonding with the conductor. The lifetime of the bending bi-metallic strip is determined by the fatigue limit of the metal alloy. Unfortunately, to the best of the authors' knowledge, very few studies exist on the Stress-Life Cycles (S–N) curve of shape memory alloys. According to Ma et al.[50], the isothermal fatigue life of a Cu–Zn–Al shape memory alloy is about 10^3 cycles, while a Ni-Mn-In-based alloy (similar to the bi-metallic material employed in this device) has a lifetime of 10^4 cycles upon high-amplitude, low-frequency thermal actuation[51]. Considering the wider temperature range of our thermal regulator, a thermal actuation lifetime of the bi-metallic strip of ~ 10^3 cycles is reasonable to assume. During our external vibration resilience testing, no performance degradation was observed even for > 10^4 low-amplitude vibration cycles.

The reliability of thermal paste can suffer from both cyclic mechanical load and long-term dry-out, causing a degradation of the thermal performance[52]. For a typical silicone-based thermal paste, Pense et al.[53] found that the thermal resistance increases about 20% during a 5000-cycle test after a long-term static test at high temperature due to the formation of voids and the propagation of cracks. This finding provides a reference for the estimation of the lifetime of the thermal paste used in the current study, as the thermal paste in the regulator is expected to undergo cyclic loading with long-term static states (ON or OFF) in-between. Hence, the lifetime of the silicone-based thermal paste employed in the thermal regulator can also be reasonably approximated with ~ 10^3 cycles, matching the lifetime of the bi-metallic strip.

As a result, the estimated lifetime of the thermal regulator is ~ 10^3 cycles. After a complete mission of the regulator, the thermal paste can be reapplied when replacing the bi-metallic strip.

Summary and conclusions

In this study, we developed and tested a new passive thermal regulator design that operates around room temperature and achieves high switching ratios in an open laboratory environment. Our regulator is structurally integer, scalable, orientation-independent, resistant to vibration, and can be easily integrated into existing thermal management solutions. One caveat of our device is the relatively high volumetric footprint and relatively high weight, which could complicate its adaption into mobile applications where weight is a constraint, such as electric vehicles, satellites, or space rovers. Its ability to maintain output temperatures well above + 10 °C, even when exposed to input temperatures as low as − 15 °C (possibly even lower, but a demonstration of the thermal performance at lower temperatures was restricted by our experimental capabilities), could make the regulator a viable option for use in stationary back-up battery energy storage or building envelopes. Furthermore, the volumetric and gravimetric footprints can be reduced by geometric optimization. To summarize, our novel passive thermal regulator design has the following performance metrics:

1. The working principle of the passive regulator is based on a bimetallic strip technology, whereas an aluminum plug attached to one end of a bimetallic strip enters and exists a wedge-shaped gap between two conductors. The regulator is fully OFF for input temperatures below ≲ 15 °C and fully ON for temperatures > 20…30 °C. The regulator was tested for input temperatures between − 15 °C and + 60 °C. In the OFF-state, output temperatures never drop below 10 °C, and in the ON-state, output temperatures are nearly identical to the input temperatures, demonstrating a very low overall thermal resistance in the design.
2. OFF-state conductances < 10 (± 5) mW/K and ON-state conductances on the order of 0.1…1.5 (± 0.08…0.3) W/K were achieved, with a time constant for switching on the order of a few minutes. The maximum demonstrated switching ratio of the regulator is 320 (± 200):1. For the fully packaged regulator, which is a more realistic model for real-life applications, we estimate a switching ratio of ≈ 40:1 from experiments and ≈ 50 $(^{+34}_{-8})$:1 from numerical simulations. The switching ratio of the fully integrated device could be further increased to ≈ 100 $(^{+18}_{-15})$:1 through geometric optimization, as indicated by numerical simulations. By changing the design to an all-aluminum regulator, the weight could be significantly reduced, achieving a gravimetric switching ratio of $SR/m \approx 250\ \mathrm{kg}^{-1}$.
3. The regulator is mechanically robust, with similar heat transfer characteristics when flipped up-side down and only a slight deterioration in performance (quantified via a 2.7 °C drop in the output temperature at an inlet temperature of ≈ − 8 °C) when mechanically vibrated at or near its resonance frequency of 22 Hz.
4. Due to the high measurement uncertainties of low heat fluxes, such as for the OFF-state, it is proposed that comparisons of ON- and OFF-state output temperature deviations from the environment, $|\Delta T_{out}|$, are a more meaningful approach to characterizing near-room temperature thermal regulators as opposed to the traditionally used switching ratio.

Data availability

The datasets generated during and/or analyzed during the current study are available from the corresponding author on reasonable request.

Received: 20 November 2023; Accepted: 15 July 2024
Published online: 23 July 2024

References

1. Mathew, J. & Krishnan, S. A review on transient thermal management of electronic devices. *J. Electron. Packag.* https://doi.org/10.1115/1.4050002 (2021).
2. Zeng, Y. *et al.* Extreme fast charging of commercial Li-ion batteries via combined thermal switching and self-heating approaches. *Nat. Commun.* **14**(1), 3229. https://doi.org/10.1038/s41467-023-38823-9 (2023).
3. Swoboda, T., Klinar, K., Yalamarthy, A. S., Kitanovski, A. & Muñoz Rojo, M. Solid-state thermal control devices. *Adv. Electron. Mater.* **7**(3), 2000625. https://doi.org/10.1002/aelm.202000625 (2021).
4. Klinar, K. & Kitanovski, A. Thermal control elements for caloric energy conversion. *Renew. Sustain. Energy Rev.* **118**, 109571. https://doi.org/10.1016/j.rser.2019.109571 (2020).
5. Depreux, L., Almanza, M., Zeggai, N., Parrain, F. & LoBue, M. Heat management and losses of electrocaloric cooling devices based on electrostatic thermal switches. *Appl. Therm. Eng.* **211**, 118290. https://doi.org/10.1016/j.applthermaleng.2022.118290 (2022).
6. Utaka, Y., Hu, K., Chen, Z. & Zhao, Y. Application of simple and effective thermal switch for solid-state magnetic refrigeration at room temperature. *Appl. Therm. Eng.* **155**, 196–205. https://doi.org/10.1016/j.applthermaleng.2019.03.127 (2019).
7. Bugby, D. C. & Rivera, J. G. High performance thermal switch for lunar and planetary surface extreme environments. *Presented at the 50th International Conference on Environmental Systems, Lisbon, Portugal* (2020).
8. Cui, H. & Overend, M. A review of heat transfer characteristics of switchable insulation technologies for thermally adaptive building envelopes. *Energy Build.* **199**, 427–444. https://doi.org/10.1016/j.enbuild.2019.07.004 (2019).
9. Wehmeyer, G., Yabuki, T., Monachon, C., Wu, J. & Dames, C. Thermal diodes, regulators, and switches: Physical mechanisms and potential applications. *Appl. Phys. Rev.* **4**(4), 041304. https://doi.org/10.1063/1.5001072 (2017).
10. Klinar, K., Swoboda, T., Muñoz Rojo, M. & Kitanovski, A. Fluidic and mechanical thermal control devices. *Adv. Electron. Mater.* **7**(3), 2000623. https://doi.org/10.1002/aelm.202000623 (2021).
11. Yang, T. *et al.* An integrated liquid metal thermal switch for active thermal management of electronics. *IEEE Trans. Compon. Packag. Manuf. Technol.* **9**(12), 2341–2351. https://doi.org/10.1109/TCPMT.2019.2930089 (2019).

12. Adams, M. J., Verosky, M., Zebarjadi, M. & Heremans, J. P. High switching ratio variable-temperature solid-state thermal switch based on thermoelectric effects. *Int. J. Heat Mass Transf.* **134**, 114–118. https://doi.org/10.1016/j.ijheatmasstransfer.2018.12.154 (2019).
13. Liu, C., Chen, Y. & Dames, C. Electric-field-controlled thermal switch in ferroelectric materials using first-principles calculations and domain-wall engineering. *Phys. Rev. Appl.* **11**(4), 044002. https://doi.org/10.1103/PhysRevApplied.11.044002 (2019).
14. Ma, J. *et al.* High performance electrostatically driven thermal switch incorporated with a mini-channel cooling. *Energy Sources Part Recovery Util. Environ. Eff.* https://doi.org/10.1080/15567036.2020.1800867 (2020).
15. Cha, G., Kim, C.-J. & Ju, Y. S. Thermal conductance switching based on the actuation of liquid droplets through the electrowetting on dielectric (EWOD) phenomenon. *Appl. Therm. Eng.* **98**, 189–195. https://doi.org/10.1016/j.applthermaleng.2015.11.098 (2016).
16. Rodrigues, C. *et al.* A magnetically-activated thermal switch without moving parts. *Energy Convers. Manag.* **197**, 111881. https://doi.org/10.1016/j.enconman.2019.111881 (2019).
17. Shi, L., Hu, Y. & He, Y. Magneto-responsive thermal switch for remote-controlled locomotion and heat transfer based on magnetic nanofluid. *Nano Energy* **71**, 104582. https://doi.org/10.1016/j.nanoen.2020.104582 (2020).
18. Chen, M. E. *et al.* Graphene-based electromechanical thermal switches. *2D Mater.* **8**(3), 035055. https://doi.org/10.1088/2053-1583/abf08e (2021).
19. Heo, H., Li, S., Bao, H. & Ju, J. A passive thermal switch with kirigami-inspired mesostructures. *Adv. Eng. Mater.* **21**(6), 1900225. https://doi.org/10.1002/adem.201900225 (2019).
20. Du, T. *et al.* Wide range continuously tunable and fast thermal switching based on compressible graphene composite foams. *Nat. Commun.* **12**(1), 4915. https://doi.org/10.1038/s41467-021-25083-8 (2021).
21. Hu, P. *et al.* Hyperelastic kevlar nanofiber aerogels as robust thermal switches for smart thermal management. *Adv. Mater.* **35**(3), 2207638. https://doi.org/10.1002/adma.202207638 (2023).
22. Yang, T. *et al.* Millimeter-scale liquid metal droplet thermal switch. *Appl. Phys. Lett.* **112**(6), 063505. https://doi.org/10.1063/1.5013623 (2018).
23. Ilic, O. *et al.* Active radiative thermal switching with graphene plasmon resonators. *ACS Nano* **12**(3), 2474–2481. https://doi.org/10.1021/acsnano.7b08231 (2018).
24. Elsahati, M., Liu, H. & Richards, R. F. Controllable thermal transport through nanoscale liquid bridging. *Appl. Phys. Lett.* **114**(18), 183104. https://doi.org/10.1063/1.5057227 (2019).
25. May, A. J. *et al.* An active convective ^{4}He heat switch. *Cryogenics* **128**, 103585. https://doi.org/10.1016/j.cryogenics.2022.103585 (2022).
26. Avanessian, T. & Hwang, G. Thermal switch using controlled capillary transition in heterogeneous nanostructures. *Int. J. Heat Mass Transf.* **121**, 127–136. https://doi.org/10.1016/j.ijheatmasstransfer.2017.12.142 (2018).
27. Kimball, M. O. *et al.* Passive gas-gap heat switches for use in low-temperature cryogenic systems. *IOP Conf. Ser. Mater. Sci. Eng.* **278**, 012010. https://doi.org/10.1088/1757-899X/278/1/012010 (2017).
28. Zou, A., Yu, F., Li, K. & Dai, W. The study of ^{4}He twin-tube convective heat switches. *Int. J. Therm. Sci.* **181**, 107747. https://doi.org/10.1016/j.ijthermalsci.2022.107747 (2022).
29. Morey, T. F. & Gorman, D. N. Development of the Viking Mars lander thermal control subsystem design. *J. Spacecr. Rockets* **13**(4), 229–236. https://doi.org/10.2514/3.57082 (1976).
30. Gilmore, D. *Spacecraft Thermal Control Handbook, Volume I: Fundamental Technologies* (American Institute of Aeronautics and Astronautics, Inc., 2002). https://doi.org/10.2514/4.989117.
31. Sunada, E., Pauken, M., Novak, K., Phillips, C., Birur, G. & Lankford, K. Design and flight qualification of a paraffin-actuated heat switch for Mars surface applications. *Presented at the International Conference On Environmental Systems*, 2002–01–2275 (2002). https://doi.org/10.4271/2002-01-2275.
32. Sunada, E., Lankford, K., Pauken, M., Novak, K. & Birur, G. Paraffin actuated heat switch for Mars surface applications. *Presented at the Space Technology and International Forum, Albuquerque, NM, USA* (2002). [Online]. https://hdl.handle.net/2014/11730.
33. Hengeveld, D., Mathison, M., Braun, J., Groll, E. & Williams, A. Review of modern spacecraft thermal control technologies. *HVACR Res.* **16**(2), 189–220. https://doi.org/10.1080/10789669.2010.10390900 (2010).
34. Ando, M., Shinozaki, K., Okamoto, A., Sugita, H. & Nohara, T. Development of mechanical heat switch for future space missions. *Presented at the 44th International Conference on Environmental Systems, Tucson, Arizona* (2014).
35. Shinozaki, K. *et al.* Research and development of heat switch for future space missions. *Trans. Jpn. Soc. Aeronaut. SPACE Sci. Aerosp. Technol. Jpn.* **12**(ists29), Po_4_7-Po_4_11. https://doi.org/10.2322/tastj.12.Po_4_7 (2014).
36. Wang, X., Tso, C. Y., Traipattanakul, B. & Chao, C. Y. H. Development of a phase change material (PCM)-based thermal switch. *HKIE Trans.* **24**(2), 107–112. https://doi.org/10.1080/1023697X.2017.1312560 (2017).
37. Kommandur, S. & Kishore, R. A. Contact-based passive thermal switch with a high rectification ratio. *ACS Eng. Au* **3**(2), 76–83. https://doi.org/10.1021/acsengineeringau.2c00046 (2023).
38. Benafan, O., Notardonato, W. U., Meneghelli, B. J. & Vaidyanathan, R. Design and development of a shape memory alloy activated heat pipe-based thermal switch. *Smart Mater. Struct.* **22**(10), 105017. https://doi.org/10.1088/0964-1726/22/10/105017 (2013).
39. Guo, L., Zhang, X., Huang, Y., Hu, R. & Liu, C. Thermal characterization of a new differential thermal expansion heat switch for space optical remote sensor. *Appl. Therm. Eng.* **113**, 1242–1249. https://doi.org/10.1016/j.applthermaleng.2016.11.102 (2017).
40. Voigt, I., Drossel, W.-G., Eppler, C., Pagel, K. & Bucht, A. Development of thermal switches based on shape memory alloy actuators. In *Volume 1: Development and Characterization of Multifunctional Materials; Modeling, Simulation, and Control of Adaptive Systems; Integrated System Design and Implementation* V001T04A028 (ASME, 2018). https://doi.org/10.1115/SMASIS2018-8263.
41. Hao, M., Li, J., Park, S., Moura, S. & Dames, C. Efficient thermal management of Li-ion batteries with a passive interfacial thermal regulator based on a shape memory alloy. *Nat. Energy* **3**(10), 899–906. https://doi.org/10.1038/s41560-018-0243-8 (2018).
42. Ma, J. *et al.* Experimental and theoretical studies of a thermal switch based on shape-memory alloy cladded with graphene paper. *Energy Sources Part Recovery Util. Environ. Eff.* **42**(7), 898–908. https://doi.org/10.1080/15567036.2019.1602202 (2020).
43. Vanapalli, S. *et al.* A passive, adaptive and autonomous gas gap heat switch. *Phys. Procedia* **67**, 1206–1211. https://doi.org/10.1016/j.phpro.2015.06.191 (2015).
44. Schneider, D., Lauer, M., Voigt, I. & Drossel, W.-G. Development and examination of switchable heat pipes. *Appl. Therm. Eng.* **99**, 857–865. https://doi.org/10.1016/j.applthermaleng.2016.01.086 (2016).
45. Van Velson, N., Tarau, C. & Anderson, W. G. Two-phase thermal switch for spacecraft passive thermal management. *Presented at the 45th International Conference on Environmental Systems, Bellevue, Washington* (2015).
46. Liu, T. *et al.* Tunable, passive thermal regulation through liquid to vapor phase change. *Appl. Phys. Lett.* **115**(25), 254102. https://doi.org/10.1063/1.5133795 (2019).
47. Liu, J. & Li, J. Design and preliminary investigation of a passive first-order magnetic phase transformation heat switch. *J. Magn. Magn. Mater.* **564**, 170183. https://doi.org/10.1016/j.jmmm.2022.170183 (2022).
48. Castelli, L. *et al.* A thermal regulator using passive all-magnetic actuation. *Cell Rep. Phys. Sci.* https://doi.org/10.1016/j.xcrp.2023.101556 (2023).
49. Webster, J. G. (ed.) The measurement, instrumentation, and sensors handbook. In *The Electrical Engineering Handbook Series* (CRC Press, 1999).
50. Ma, S., Zhang, X., Zheng, G., Qian, M. & Geng, L. Toughening of Ni–Mn-based polycrystalline ferromagnetic shape memory alloys. *Materials* **16**(16), 5725. https://doi.org/10.3390/ma16165725 (2023).

51. Pfeuffer, L. *et al.* Microstructure engineering of metamagnetic Ni–Mn-based Heusler compounds by Fe-doping: A roadmap towards excellent cyclic stability combined with large elastocaloric and magnetocaloric effects. *Acta Mater.* **221**, 117390. https://doi.org/10.1016/j.actamat.2021.117390 (2021).
52. Carlton, H., Pense, D. & Huitink, D. Thermomechanical degradation of thermal interface materials: Accelerated test development and reliability analysis. *J. Electron. Packag.* **142**(3), 031112. https://doi.org/10.1115/1.4047099 (2020).
53. Pense, D., Carlton, H. & Huitink, D. Thermo-mechanical degradation of thermal interface materials: Accelerated test development and reliability analysis. In *ASME 2019 International Technical Conference and Exhibition on Packaging and Integration of Electronic and Photonic Microsystems* V001T06A009 (American Society of Mechanical Engineers, 2019). https://doi.org/10.1115/IPACK2019-6416.

Acknowledgements
This work was supported by an Early Career Faculty grant from NASA's Space Technology Research Grants Program (Grant No. 80NSSC20K0072).

Author contributions
S.P. conducted most of the experiments, analyzed the data, conducted numerical simulations, and wrote most of the manuscript. J.L. and P.B.W. conceived the project, assisted with data collection and analysis, and edited the manuscript.

Competing interests
The authors declare no competing interests.

Additional information
Supplementary Information The online version contains supplementary material available at https://doi.org/10.1038/s41598-024-67758-4.

Correspondence and requests for materials should be addressed to P.B.W.

Reprints and permissions information is available at www.nature.com/reprints.

Publisher's note Springer Nature remains neutral with regard to jurisdictional claims in published maps and institutional affiliations.